Proceedings of the Institute of Acoustics

INVARIANT PARAMETER ESTIMATION ACROSS VARYING SEABEDS IN SYNTHETIC APERTURE SONAR IMAGERY

Chao Chen University of Missouri, Columbia, MO, USA
Alina Zare University of Missouri, Columbia, MO, USA
J. Tory Cobb Naval Surface Warfare Center, Panama City Beach, FL, USA

1 INTRODUCTION

Side-look synthetic aperture sonar (SAS) can produce very high quality images of the seabed. The imagery generated by SAS sensors display the seafloor and associated textures, such as sand ripples or seagrass[1]. The characterization of SAS imagery is important for applications such as the detection and classification of targets[2,3], seabed segmentation and classification[4–6], and others[7–9]. In this paper, we seek to estimate invariant features of the seafloor to describe and distinguish between seafloor types. Our approach makes the assumption that the local characteristics of the true bathymetry of the seafloor can be represented by a Gaussian Markov Random Field (GMRF). Since we characterize the bathymetry of the seafloor, this method yields GMRF parameters that are invariant to acoustic sensing modality and geometry.

High-quality SAS imagery has prompted the development of algorithms for the detection and classification of targets[2,3], seabed segmentation and classification[4–6], and others[7–9]. In the majority of these methods, SAS imagery are analyzed by considering features that describe image intensity and texture, (e.g, statistical features[10–23] or shape descriptors[22,23]). For example, Guillaudeux and Daniel[10] used two features, namely, intensity mean and variance which are computed over pixel intensities within a small window to segment sonar imagery. Maussang et al. included higher-order statistics (e.g., kurtosis and skewness)[11–15] for small target detection, underwater mine classification and detection, and echo detection. Cobb and Slatton used the K-distribution shape parameter as well as autocorrelation functions as features to segment SAS images[16,18]. Mignotte et al.[19] proposed a hierarchical segmentation procedure to separate shadow and sea bottom reverberation using a hierarchical Markov Random Field (MRF) model which combines coarse-to-fine interactions with a spatial neighborhood structure. Reed et al.[20,21] also used an MRF model to segment sidescan sonar images into three different regions: highlights, shadows of objects and general background.

However these intensity-based features can be degraded due to the speckle noise present in the sonar imagery and vary drastically with the sensing geometry. Given a particular sensing geometry and bathymetry, the textures and pixel values imaged by a SAS system will vary over the same spatial region of the seafloor. Features based on image characteristics are often not quantifying invariant parameters of the seafloor but, instead, are describing the relationship of that particular sensing geometry with respect to that area of the seafloor. A different pass of the SAS sensor with varying range and aspect angle over the same region may result in very different image-based features. In this paper, we investigate the use of Gaussian Markov Random Fields (GMRFs) to characterize the underlying bathymetry depicted in a SAS image. In order to estimate the GMRF parameters that describe the bathymetry of a region, bathymetry slope values for imaged seafloor are needed. However, many of the pixels on the seafloor are shadowed and, thus, much of the information related to their heights relative to neighboring pixels is unknown. To address this issue, an Expectation Maximization algorithm is used to estimate the GMRF parameters. The proposed method can be divided into four main steps summarized in Fig. 1.

This paper is organized as follows. In Section 2, we detail our approach to estimate the slope of the bathymetry of every unoccluded pixel in the image. Section 3 presents the proposed EM algorithm that estimates bathymetry parameters and refines the bathymetry profile. Experimental results obtained by the proposed method are reported and analyzed in Section 4 along with comparisons to those obtained by three other GMRF parameter estimation methods.

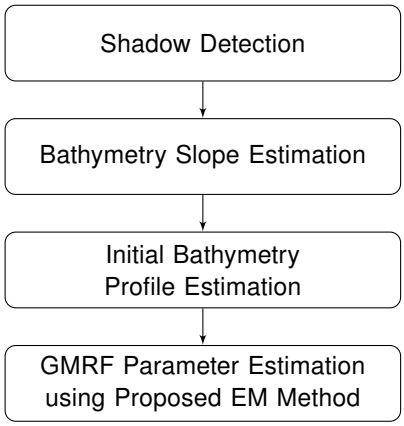

Fig. 1. Flowchart of the Proposed Method

2 ESTIMATING THE RELATIVE BATHYMETRY PROFILE

Incident acoustic waves of SAS will be reflected and scattered from the seafloor. The component that is backscattered towards the sonar will be collected by the sonar receivers and contribute to the formation of the SAS imagery. Here, SAS imagery have been modeled with an intensity representation of the backscattered acoustic energy given a specific range, depression and aspect angle[24]. Given knowledge of the backscattering model with appropriate assumptions, the intensity image can be converted into the bathymetry map[25]. A challenge in this conversion comes from the shadowed pixels where the incident acoustic wave is blocked by the preceding contour and, thus, no bathymetry information are available for these pixels. In our work, we determine locations of the shadowed pixels based on the local mean and variance and compute an estimate of slope of the bathymetry for non-shadowed pixels using the variation of local pixel intensity.

2.1 Shadow Detection

Our current approach for identifying occluded pixels is to apply a local mean and variance filter to the input image. Shadowed/occluded regions have both a small local mean and low variance. Thus, after computing the mean and variance in a local window $\mathscr{W}$ surrounding each pixel, the mean and variance values are thresholded with predetermined, fixed values. If both the mean and variance are below their respective thresholds, the pixel is labeled as a shadowed or occluded pixel.

2.2 Backscattering Model: Lambertian Reflectance Model

In order to estimate the bathymetry, we need a backscattering model relating intensity to bathymetry. Seafloor backscattering is a complicated phenomenon, which is generally considered to be composed of a combination of surface and volume scattering, (i.e., roughness interface scattering and scattering from inhomogeneities within the sediment volume[26,27]). However, for simplicity, in our work a Lambertian reflectance model is applied as the backscattering model[27–29]. Under the Lambertian reflectance model, image intensity $I_{i,j}$ is the cosine of the angle between the seafloor orientation (normal vector) $\mathbf{N}_{i,j}$ and the incident acoustic wave direction $\mathbf{L}_{i,j}$ at the seafloor location corresponding to pixel (i,j)[29]. This model is illustrated in Fig. 2.

The SAS image intensity can be expressed as

$$I_{i,j} = \cos(\alpha) = \frac{\langle \mathbf{L}_{i,j}, \mathbf{N}_{i,j} \rangle}{\langle \mathbf{L}_{i,j}, \mathbf{L}_{i,j} \rangle \cdot \langle \mathbf{N}_{i,j}, \mathbf{N}_{i,j} \rangle}, \tag{1}$$

with

$$\mathbf{L}_{i,j} = \begin{pmatrix} j \\ 0 \\ -A_H + H_{i,j} \end{pmatrix} \simeq \begin{pmatrix} j \\ 0 \\ -A_H \end{pmatrix}, \text{ and } \mathbf{N}_{i,j} = \begin{pmatrix} -\partial H/\partial j \\ -\partial H/\partial i \\ 1 \end{pmatrix} \simeq \begin{pmatrix} -\Delta H_{i,j}/\Delta R \\ 0 \\ 1 \end{pmatrix}, \tag{2}$$

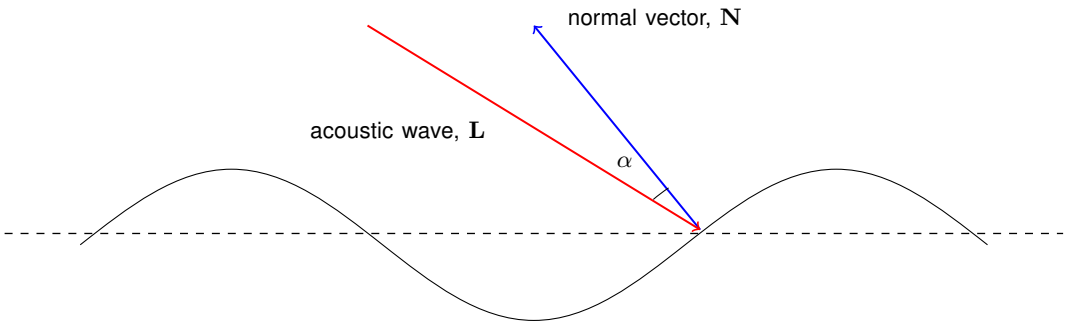

Fig. 2. Graphic Depiction of the Lambertian Reflectance Model.

where A_H is the sonar height, $H_{i,j}$ is the absolute bathymetry value corresponding to pixel (i,j), ΔR is the sonar range resolution and $\Delta H_{i,j}$ is the bathymetry slope at (i,j). In our data, A_H is usually around $5m$ and $H_{i,j}$ is generally smaller than $10cm$ ($H_{i,j} \ll A_H$). Thus, the component $-A_H + H_{i,j}$ in $\mathbf{L}_{i,j}$ can be approximated by $-A_H$. Using this approximation yields an expression that depends only on relative change in $H_{i,j}$ rather than absolute bathymetry values. As described in the following Section 2.3, $\Delta H_{i,j}$ can be estimated using (1)-(2) given $I_{i,j}$, A_H and ΔR.

2.3 Initial Bathymetry Estimation

Since input SAS imagery are generally not calibrated, intensity information does not provide any absolute bathymetry information. Therefore, only bathymetry slope information can be estimated from the input image. Pixel intensity is an indicator of slope information of the seafloor, which can potentially provide a relative change in height at each pixel[30]. A large intensity value generally indicates a steeper seafloor slope (e.g., maximal values are perpendicular to the grazing angle from the sensor). A small value indicates a shallow seafloor slope. Given an assumed value for the first pixel in each row of the image and the first pixel following any occluded region, a bathymetry slope profile for all of the observed pixels can be estimated based on the relative intensity of each pixel. Essentially, all intensity values for observed pixels are normalized and used as a slope estimate (change from the bathymetry value of the preceding pixel) to estimate the bathymetry profile of observed pixels. In this initial estimate, shadowed pixels are set to have a bathymetry slope of -2. From (1) - (2) and this naive interpolation scheme, the bathymetry slope can be estimated as

$$\Delta H_{i,j} = \begin{cases} \dfrac{\Delta R}{\tan(\arctan(\frac{A_H}{j}) + \arccos(I_{i,j}))} & \text{if } M_{i,j} = 0, \\ -2 & \text{otherwise,} \end{cases} \tag{3}$$

where $M_{i,j}$ is the shadow map at pixel (i,j) such that $M_{i,j} = 1$ if pixel (i,j) is shadowed/occluded and $M_{i,j} = 0$ otherwise. Given (3), the estimated bathymetry profile will be

$$\hat{H}_{i,j} = \sum_{k=1}^{j} \Delta H_{i,k}, \tag{4}$$

which is the cumulative sum of the bathymetry slope along the range direction. The first column in the image is assumed to be the reference height, which means that $\Delta H_{i,1} = I_{i,1}$.

3 GMRF PARAMETER ESTIMATION AND BATHYMETRY SLOPE REFINEMENT

Once an initial bathymetry profile for the observed pixels is estimated as described above, then the GMRF parameters for that bathymetry profile can be estimated. We use an Expectation-Maximization (EM)[31,32] with an Iterated Conditional Modes (ICM)[32,33] approach. In our approach, we assume that our initial estimated bathymetry profile is inaccurate. Thus, the proposed algorithm aims both to refine the bathymetry profile in the Expectation step (E-step) and update the GMRF parameters in the Maximization

step (M-step). The algorithm is summarized in the pseudo-code in Algorithm 1. Each step of the proposed approach is described in the following sub-sections as indicated in Algorithm 1.

Algorithm 1 *Proposed EM with ICM algorithm*

Input: Shadow map $M_{i,j}$ and initial bathymetry map $\hat{H}$.

1: Initialize σ_0^2, σ_1^2, the bathymetry map, H, and the GMRF parameters, $\boldsymbol{\beta}$.

M-Step:

2: Estimate σ_1^2 by $\hat{\sigma}_1^2 = \arg\max_{\sigma_1^2} P(\hat{H}|H, \sigma_1^2)$ (Section 3.1).

3: Estimate σ_0^2 by $\hat{\sigma}_0^2 = \arg\max_{\sigma_0^2} P(\hat{H}|H, \sigma_0^2)$ (Section 3.1).

4: Estimate $\boldsymbol{\beta}$ by $\bar{\boldsymbol{\beta}} = \arg\max_{\boldsymbol{\beta}} P(H|\boldsymbol{\beta})$. MPLE is used to maximize the PL likelihood function (Section 3.2).

E-Step:

5: Update H by $H = \arg\max_H P(H|\hat{H}, \boldsymbol{\beta}, \sigma_0^2, \sigma_1^2)$ based on the current $\hat{H}$, $\boldsymbol{\beta}$, σ_0^2 and σ_1^2. The maximization here is performed by using ICM method (Section 3.3).

6: Return to step 2 for a fixed number of iterations or until convergence.

3.1 Bathymetry Profile Distortion Model Parameter Estimation

The bathymetry profile estimate is refined by considering this as an image restoration problem using the current estimated GMRF model[34,35]. In our work, due to occurrence of shadowed pixels, we consider two types of possible bathymetry profile errors, namely, occlusion error and reconstruction error. Occlusion error is found at the shadowed pixels where any bathymetry information has been concealed and, thus, bathymetry is initially only estimated by the naive interpolation scheme described in Equation (3). Reconstruction error represents all the other possible errors such as noise in the sonar image or error due to the backscattering model. We treat the occlusion error and reconstruction error as two zero-mean Gaussian random variables with different variances. Given this model, the bathymetry profile distortion model can be expressed as

$$\hat{H}_{i,j} = H_{i,j} + e_{i,j}, \tag{5}$$

where $e_{i,j} \sim \mathcal{N}(0, \sigma_{i,j}^2)$ is the independent zero-mean Gaussian error which distorts the true bathymetry map, H. We assume that occlusion error occurs at only shadowed pixels and reconstruction error occurs only at the remaining pixels,

$$e_{i,j} \sim \begin{cases} \mathcal{N}(0, \sigma_1^2) & \text{if } M_{i,j} = 1, \\ \mathcal{N}(0, \sigma_0^2) & \text{otherwise,} \end{cases} \tag{6}$$

where $e_{i,j} \sim \mathcal{N}(0, \sigma_1^2)$ represents occlusion error and $e_{i,j} \sim \mathcal{N}(0, \sigma_0^2)$ reconstruction error.

Following the conditional independence assumption[33] that given H, all the elements in $\hat{H}$ are conditionally independent and that each element of $\hat{H}_{i,j}$ has a known conditional density function $\mathcal{N}(\hat{H}_{i,j}|H_{i,j}, \sigma_{i,j}^2)$, then the conditional density of $\hat{H}$ given H can be simplified to

$$\begin{aligned} P(\hat{H}|H) &= \prod_{\forall(i,j)} p(\hat{H}_{i,j}|H_{i,j}, M_{i,j}) = \prod_{\substack{(i,j):\\ M_{i,j}=1}} p(\hat{H}_{i,j}|H_{i,j}) \prod_{\substack{(i,j):\\ M_{i,j}=0}} p(\hat{H}_{i,j}|H_{i,j}) \\ &= \prod_{\substack{(i,j):\\ M_{i,j}=1}} \mathcal{N}(\hat{H}_{i,j}|H_{i,j}, \sigma_1^2) \prod_{\substack{(i,j):\\ M_{i,j}=0}} \mathcal{N}(\hat{H}_{i,j}|H_{i,j}, \sigma_0^2). \end{aligned} \tag{7}$$

Then, the distortion model parameters σ_1^2 and σ_0^2 can be estimated using Maximum likelihood estimation (MLE). By maximizing (7), the update equations for σ_1^2 and σ_0^2 are

$$\hat{\sigma}_1^2 = \frac{1}{m_1} \sum_{\substack{(i,j):\\ M_{i,j}=1}} [H_{i,j} - \hat{H}_{i,j}]^2, \tag{8}$$

and

$$\hat{\sigma}_0^2 = \frac{1}{m_0} \sum_{\substack{(i,j):\\ M_{i,j}=0}} [H_{i,j} - \hat{H}_{i,j}]^2, \tag{9}$$

respectively, where m_1 is the number of shadowed pixels and m_0 non-shadowed pixels.

3.2 Gaussian Markov Random Fields (GMRFs) Model Parameter Estimation

In step 4 of Algorithm 1, the GMRF parameters, $\boldsymbol{\beta}$, are updated. As stated previously, these parameters are the desired invariant seafloor features. In our implementation, we adopt a 2nd-order homogeneous GMRF model with four spatial interaction parameters $\boldsymbol{\beta} = (\beta_1, \beta_2, \beta_3, \beta_4)^T$. As shown in Fig. 3, β_1 and β_2 are for neighbors which are one pixel apart horizontally and vertically, and β_3 and β_4 for diagonally adjacent neighbors in southeast and southwest directions[36]. The local conditional probability density function (pdf) is defined as

$$H_{i,j}|H_{\mathcal{N}_{i,j}} \sim \mathcal{N}\left((w_{i,j}H)^T\boldsymbol{\beta}, \sigma^2\right), \tag{10}$$

with

$$(w_{i,j}H) = \left[(H_{i,j-1} + H_{i,j+1}), (H_{i-1,j} + H_{i+1,j}), (H_{i-1,j-1} + H_{i+1,j+1}), (H_{i+1,j-1} + H_{i-1,j+1})\right]^T, \tag{11}$$

where $w_{i,j}$ is an indicator matrix which selects the neighbors of pixel (i, j) and σ^2 is the local variance which is usually assumed to be known.

For GMRF parameter estimation, Maximum likelihood estimation (MLE) is computationally demanding particularly for large lattices. Besag[37,38] proposed the Maximum pseudo-likelihood estimation (MPLE) as an alternative to MLE, where the pseudo-likelihood (PL) is defined as the product of the local conditional pdfs of each pixel given the neighbors[36–39]. In our approach, we employ the MPLE method to estimate the $\boldsymbol{\beta}$ GMRF parameters. Note that the MPLE approach is used to estimate the $\boldsymbol{\beta}$ parameters only. The log-PL is defined as

$$\mathbf{ln}PL(H) = -\frac{1}{2}MNln(2\pi\sigma^2) - \frac{1}{2\sigma^2}\sum_{i=1}^{N}\sum_{j=1}^{M}(H_{i,j} - (w_{i,j}H)^T\boldsymbol{\beta})^2, \tag{12}$$

and, given this model, the GMRF parameter update equations are

$$\bar{\boldsymbol{\beta}} = \left(\sum_{i=1}^{N}\sum_{j=1}^{M}(w_{i,j}H)(w_{i,j}H)^T\right)^{-1}\left(\sum_{i=1}^{N}\sum_{j=1}^{M}(w_{i,j}H)H_{i,j}\right), \tag{13}$$

and

$$\bar{\sigma^2} = \frac{1}{MN}\sum_{i=1}^{N}\sum_{j=1}^{M}\left(H_{i,j} - (w_{i,j}H)\bar{\boldsymbol{\beta}}\right)^2. \tag{14}$$

β_3	β_2	β_4
β_1		β_1
β_4	β_2	β_3

Fig. 3. The 2nd-order Neighborhood Structure

3.3 Bathymetry Profile Refinement

After parameter estimation for the distortion and GMRF models, the proposed approach refines the bathymetry profile according to all available information; that is, find the H that maximizes the conditional probability $p(H|\hat{H})$. Probabilistic solutions for this problem, such as simulated annealing, the Gibbs sampler, or the Metropolis algorithm, ensure the convergence toward a global maximum but have computational costs[40]. Thus, we employ a deterministic algorithm called Iterated Conditional Modes (ICM)[33] which lightens the computational burden by providing a suboptimal solution that sequentially maximizes local conditional probabilities, $p\left(H_{i,j}|\hat{H}, H_{\mathcal{N}_{i,j}}\right)$.

From the assumptions that the observed $\hat{H}_{i,j}$ are conditionally independent given H, and that each $\hat{H}_{i,j}$ has the conditional density function $p\left(\hat{H}_{i,j}|H_{i,j}\right)$ dependent only on $H_{i,j}$, it follows that

$$p\left(H_{i,j}|\hat{H}, H_{\mathcal{N}_{i,j}}\right) \propto p\left(\hat{H}_{i,j}|H_{i,j}\right) p\left(H_{i,j}|H_{\mathcal{N}_{i,j}}\right). \tag{15}$$

Maximizing Equation (15) is equivalent to minimizing the the following potential

$$V_{i,j} = \frac{1}{2\sigma_{i,j}^2}\left(H_{i,j} - \hat{H}_{i,j}\right)^2 + \frac{1}{2\sigma^2}\left(H_{i,j} - \sum_{i,k\in\mathcal{N}_{i,j}} \beta_{i,k} H_{i,k}\right)^2, \tag{16}$$

where the first term enforces the assumption that our distortion model is Gaussian distributed and the second term minimizes the difference between neighboring pixels. ICM evaluates the second term given $H_{i,k}$ from the last iteration. Using the method of Lagrange multipliers, the update equation for $H_{i,j}$ at iteration $(t+1)$ is given by

$$H_{i,j}^{(t+1)} = \frac{\sigma^2}{\sigma_{i,j}^2 + \sigma^2}\hat{H}_{i,j} + \frac{\sigma_{i,j}^2}{\sigma_{i,j}^2 + \sigma^2} \sum_{i,k\in\mathcal{N}_{i,j}} \beta_{i,k} H_{i,k}^{(t)}. \tag{17}$$

4 EXPERIMENTS

In order to evaluate our estimated GMRF parameter, two sets of experiments were conducted. The first experiment examined the ability for the proposed algorithm to recover true bathymetry GMRF parameters given varying sonar aspect angles. The second experiment examined the ability of the proposed method to estimate parameters that can distinguish between different sea floor types.

4.1 Experiment I - Invariant to SAS System Height

The first set of experiments investigates the stability of the approach to estimate the correct GMRF parameter while varying SAS system aspect angles. With a fixed underlying true bathymetry map, SAS imagery were simulated. Then, the proposed EM approach was applied to each simulated image and the estimated GMRF parameters were compared to the true values.

In this experiment, the sonar system was set to three different heights resulting three different sensing geometries. Each sensing geometry was used to simulated SAS imagery with two different GMRF parameter sets, namely, [0.5108, 0.4107, 0.2097, 0.2097], and [0.5432, 0.2910, 0.1580, 0.1580]. For each parameter set, 10 simulations of 513-by-513 images were generated. Then, given these simulated data set, the proposed algorithm was applied and the GMRF parameters were estimated. In Table I and Table II, the average squared error (standard deviation) is computed over 10 runs. Our proposed algorithm (denoted by EM(s)) is compared to three other methods, namely, MPLE, Coding method and EM(e). This experiment shows that, even with varying sensing geometry, stable GMRF parameters for the underlying bathymetry are estimated. With respect to the estimation error, our proposed EM algorithm achieves the best performance among the four methods.

4.2 Experiment II

The second set of experiments investigates the value of the GMRF parameters with respect to distinguishing between different seabed types. In this experiment, GMRF parameters are estimated from several manually selected and labeled sub-images from real SAS data. Since our data set was unlabeled with respect to seafloor type, the following labeling process was used. Each extracted sub-image from real SAS data was labeled by three individuals separately. The true label was determined to be the seafloor type that was agreed by all the three individuals. Samples in which all three individuals did not assign the same label were removed from the data set. Samples of two seafloor types considered are shown in Fig. 4. The dataset contains 104 sub-images categorized into two classes: sand ripple and hard-pack sand. The sand ripple class has 60 sub-images and the hard-pack sand class has 44 sub-images. For each sub-image, the GMRF parameters were estimated with the proposed approach. These GMRF parameters

TABLE I
Average Squared Error (Standard Deviation) of Estimates Over 10 Simulations of the 1st Parameter Set.

Method	SP	$\beta_1 = 0.5108$	$\beta_2 = 0.4107$	$\beta_3 = 0.2097$	$\beta_4 = 0.2097$
EM(s)	P_1	$\mathbf{1.06 \times 10^{-4}}(2.93 \times 10^{-5})$	$\mathbf{1.96 \times 10^{-4}}(2.50 \times 10^{-3})$	$\mathbf{1.25 \times 10^{-4}}(1.30 \times 10^{-3})$	$\mathbf{1.20 \times 10^{-4}}(1.50 \times 10^{-3})$
	P_2	$\mathbf{1.05 \times 10^{-4}}(2.30 \times 10^{-5})$	$1.65 \times 10^{-4}(1.70 \times 10^{-3})$	$\mathbf{6.79 \times 10^{-6}}(6.58 \times 10^{-4})$	$\mathbf{6.09 \times 10^{-4}}(1.40 \times 10^{-3})$
	P_3	$\mathbf{1.07 \times 10^{-4}}(1.79 \times 10^{-5})$	$\mathbf{2.67 \times 10^{-6}}(1.40 \times 10^{-3})$	$\mathbf{1.20 \times 10^{-5}}(8.28 \times 10^{-4})$	$\mathbf{1.72 \times 10^{-5}}(1.00 \times 10^{-3})$
EM(e)	P_1	$1.07 \times 10^{-4}(2.89 \times 10^{-5})$	$1.20 \times 10^{-3}(2.20 \times 10^{-3})$	$4.70 \times 10^{-4}(1.10 \times 10^{-3})$	$4.57 \times 10^{-4}(1.30 \times 10^{-3})$
	P_2	$1.06 \times 10^{-4}(2.23 \times 10^{-5})$	$\mathbf{1.48 \times 10^{-4}}(1.60 \times 10^{-3})$	$9.91 \times 10^{-5}(6.16 \times 10^{-4})$	$1.09 \times 10^{-4}(1.30 \times 10^{-3})$
	P_3	$1.08 \times 10^{-4}(1.48 \times 10^{-5})$	$4.07 \times 10^{-4}(1.20 \times 10^{-3})$	$1.92 \times 10^{-4}(8.68 \times 10^{-4})$	$2.13 \times 10^{-4}(9.13 \times 10^{-4})$
MPLE	P_1	$1.14 \times 10^{-4}(1.49 \times 10^{-5})$	$3.04 \times 10^{-2}(1.60 \times 10^{-3})$	$8.40 \times 10^{-3}(1.10 \times 10^{-3})$	$8.30 \times 10^{-3}(1.00 \times 10^{-3})$
	P_2	$1.14 \times 10^{-4}(6.95 \times 10^{-6})$	$2.19 \times 10^{-2}(1.40 \times 10^{-3})$	$6.10 \times 10^{-3}(7.15 \times 10^{-4})$	$6.20 \times 10^{-3}(1.20 \times 10^{-3})$
	P_3	$1.15 \times 10^{-4}(6.38 \times 10^{-6})$	$1.80 \times 10^{-2}(1.20 \times 10^{-3})$	$5.00 \times 10^{-3}(7.84 \times 10^{-4})$	$5.10 \times 10^{-3}(9.28 \times 10^{-4})$
Coding	P_1	$1.14 \times 10^{-4}(1.51 \times 10^{-5})$	$3.04 \times 10^{-2}(1.60 \times 10^{-3})$	$8.40 \times 10^{-3}(1.10 \times 10^{-3})$	$8.30 \times 10^{-3}(1.00 \times 10^{-3})$
	P_2	$1.14 \times 10^{-4}(7.03 \times 10^{-6})$	$2.19 \times 10^{-2}(1.40 \times 10^{-3})$	$6.10 \times 10^{-3}(7.15 \times 10^{-4})$	$6.20 \times 10^{-3}(1.20 \times 10^{-3})$
	P_3	$1.15 \times 10^{-4}(6.48 \times 10^{-6})$	$1.80 \times 10^{-2}(1.20 \times 10^{-3})$	$5.00 \times 10^{-3}(7.84 \times 10^{-4})$	$5.10 \times 10^{-3}(9.31 \times 10^{-4})$

EM(s) is the proposed method. EM(e) is similar to EM(s) but treats reconstruction and occlusion error equally, i.e., $\sigma_0^2 = \sigma_1^2$. MPLE is maximum pseudo-likelihood estimation method[37] and Coding is the Coding method[41].

TABLE II
Average Squared Error (Standard Deviation) of Estimates Over 10 Simulations of the 2nd Parameter Set.

Method	SP	$\beta_1 = 0.5432$	$\beta_2 = 0.2910$	$\beta_3 = 0.1580$	$\beta_4 = 0.1580$
EM(s)	P_1	$\mathbf{1.80 \times 10^{-3}}(2.95 \times 10^{-5})$	$\mathbf{1.51 \times 10^{-5}}(3.60 \times 10^{-3})$	$\mathbf{1.47 \times 10^{-4}}(2.30 \times 10^{-3})$	$\mathbf{1.29 \times 10^{-4}}(1.80 \times 10^{-3})$
	P_2	$\mathbf{1.80 \times 10^{-3}}(4.22 \times 10^{-5})$	$1.10 \times 10^{-3}(3.40 \times 10^{-3})$	$\mathbf{1.85 \times 10^{-5}}(1.60 \times 10^{-3})$	$\mathbf{2.26 \times 10^{-5}}(2.20 \times 10^{-3})$
	P_3	$\mathbf{1.80 \times 10^{-3}}(1.52 \times 10^{-5})$	$5.15 \times 10^{-4}(2.90 \times 10^{-3})$	$\mathbf{3.99 \times 10^{-6}}(1.70 \times 10^{-3})$	$\mathbf{4.26 \times 10^{-6}}(1.80 \times 10^{-3})$
EM(e)	P_1	$1.80 \times 10^{-3}(2.91 \times 10^{-5})$	$3.42 \times 10^{-4}(3.20 \times 10^{-3})$	$4.75 \times 10^{-4}(2.20 \times 10^{-3})$	$4.47 \times 10^{-4}(1.40 \times 10^{-3})$
	P_2	$1.80 \times 10^{-3}(4.07 \times 10^{-5})$	$\mathbf{7.27 \times 10^{-5}}(3.10 \times 10^{-3})$	$7.22 \times 10^{-5}(1.60 \times 10^{-3})$	$7.11 \times 10^{-5}(2.00 \times 10^{-3})$
	P_3	$1.80 \times 10^{-3}(1.51 \times 10^{-5})$	$\mathbf{1.13 \times 10^{-5}}(3.30 \times 10^{-3})$	$1.49 \times 10^{-4}(2.00 \times 10^{-3})$	$1.50 \times 10^{-4}(1.80 \times 10^{-3})$
MPLE	P_1	$1.90 \times 10^{-3}(1.43 \times 10^{-5})$	$1.76 \times 10^{-2}(2.50 \times 10^{-3})$	$6.30 \times 10^{-3}(1.80 \times 10^{-3})$	$6.10 \times 10^{-3}(1.20 \times 10^{-3})$
	P_2	$1.90 \times 10^{-3}(1.89 \times 10^{-5})$	$1.23 \times 10^{-2}(2.40 \times 10^{-3})$	$4.60 \times 10^{-3}(1.40 \times 10^{-3})$	$4.60 \times 10^{-3}(1.60 \times 10^{-3})$
	P_3	$1.90 \times 10^{-3}(8.51 \times 10^{-6})$	$1.01 \times 10^{-2}(2.60 \times 10^{-3})$	$3.90 \times 10^{-3}(1.70 \times 10^{-3})$	$3.90 \times 10^{-3}(1.50 \times 10^{-3})$
Coding	P_1	$1.80 \times 10^{-3}(1.42 \times 10^{-5})$	$1.76 \times 10^{-2}(2.50 \times 10^{-3})$	$6.30 \times 10^{-3}(1.80 \times 10^{-3})$	$6.10 \times 10^{-3}(1.20 \times 10^{-3})$
	P_2	$1.90 \times 10^{-3}(1.88 \times 10^{-5})$	$1.23 \times 10^{-2}(2.40 \times 10^{-3})$	$4.60 \times 10^{-3}(1.40 \times 10^{-3})$	$4.60 \times 10^{-3}(1.70 \times 10^{-3})$
	P_3	$1.90 \times 10^{-3}(8.33 \times 10^{-6})$	$1.01 \times 10^{-2}(2.60 \times 10^{-3})$	$3.90 \times 10^{-3}(1.70 \times 10^{-3})$	$3.90 \times 10^{-3}(1.40 \times 10^{-3})$

were then used as features in KNN classifier trained to distinguish between the two seafloor types. For the KNN classifier, we varied K from 3 to 9 with step-size 2 and the decision rule was majority-vote. The performance was measured using a two-fold cross-validation scheme. The sub-images are assigned into two equal size sets. Each set is consist of the randomly selected half samples of the two classes. 1000 rounds of validations are performed, and the validation results are averaged over the rounds.

A practical problem in this experiment is downsampling of the sub-images. SAS images have very high resolution (e.g., on the order of centimeters per pixel). The physical distance between adjacent pixels in SAS imagery is very small, which indicates a high order GMRF with a large amount of parameters. To reduce the computational complexity and make the images fit with the proposed 2nd-order GMRF, the sub-images were downsampled. Since the optimal downsampling rate is hard to determine, we conducted experiments in which the downsampling rate was varied from 1 to 10. Experimental results are shown in Table III. The best classification results occur when the downsampling rate is 5 and the classification accuracy at this rate is around 80%. This experiment validates the value of the GMRF parameters to describe varying seafloor types.

TABLE III
Validation Results with Different K and Downsampling Rates

Downsampling Rate	1	2	3	4	5
$K = 3$	56.12%(55.55%)	54.06%(54.23%)	62.04%(61.62%)	76.87%(75.29%)	**79.38%(77.82%)**
$K = 5$	57.20%(56.20%)	56.06%(54.89%)	62.77%(61.57%)	79.09%(77.49%)	**80.45%(78.71%)**
$K = 7$	58.25%(57.09%)	55.70%(54.73%)	62.15%(60.43%)	79.87%(78.39%)	**80.97%(79.12%)**
$K = 9$	58.05%(56.82%)	55.56%(54.14%)	61.23%(59.90%)	81.04%(79.15%)	**81.21%(79.71%)**

Downsampling Rate	6	7	8	9	10
$K = 3$	76.53%(75.42%)	78.68%(77.74%)	78.60%(77.80%)	76.32%(75.09%)	76.18%(74.59%)
$K = 5$	78.15%(76.94%)	79.67%(78.04%)	79.41%(77.85%)	74.05%(72.41%)	72.22%(70.87%)
$K = 7$	78.91%(77.42%)	80.01%(78.62%)	79.21%(77.86%)	71.79%(70.10%)	68.41%(67.16%)
$K = 9$	79.16%(77.74%)	80.92%(78.65%)	79.32%(77.59%)	70.61%(69.58%)	65.72%(64.56%)

Numbers outside parentheses are classification accuracy for the first fold, and numbers in parentheses are for the second fold.

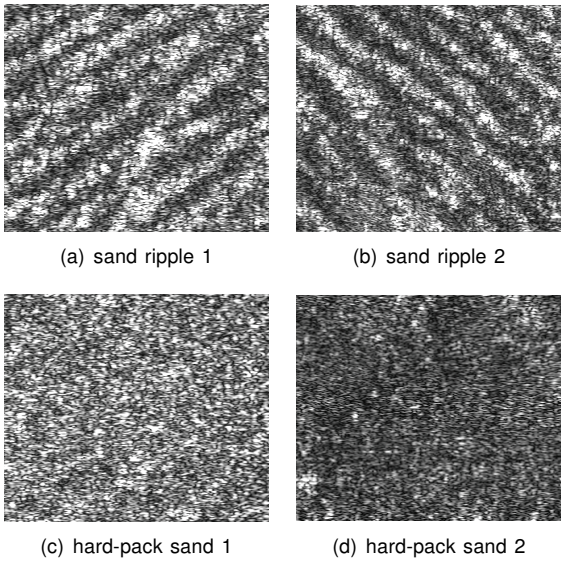

(a) sand ripple 1 (b) sand ripple 2

(c) hard-pack sand 1 (d) hard-pack sand 2

Fig. 4. Samples of different seabed types. (a)-(b): sand ripple samples, (c)-(d): hard-pack sand samples.

5 SUMMARY AND FUTURE WORK

This paper presents a set of invariant and discriminative features describing the local characteristics of the bathymetry map and proposes an EM with ICM method to extract these features. The proposed EM with ICM algorithm provides reliable GMRF parameters, and the developed feature is shown to be invariant to the sensing geometry and applicable to seafloor classification tasks.

Our future work will include many extensions to and further investigation of the proposed method. For example, the current distortion is modeled to be Gaussian distributed. Future work will include expanding the distortion model to consider more applicable error distributions. ICM methods depends highly on initialization and investigation into a better initialization scheme will be developed in the future. Furthermore, investigation can be conducted into the applicability of the GMRF model on the range of possible seabed bathymetry profiles as well as the applicability of the proposed invariant features extracted from Interferometric SAS.

6 ACKNOWLEDGEMENTS

The authors graciously thank the Office of Naval Research, Code 321, for funding this research. Any opinions, findings, and conclusions or recommendations expressed in this material are those of the author(s) and do not necessarily reflect the views of the Office of Naval Research.

7 REFERENCES

1. J. T. Cobb, K. C. Slatton, and G. J. Dobeck, “A parametric model for characterizing seabed textures in synthetic aperture sonar images,” *Oceanic Engineering, IEEE Journal of*, vol. 35, no. 2, pp. 250–266, 2010.
2. G. J. Dobeck, “Algorithm fusion for automated sea mine detection and classification,” in *IEEE OCEANS*, vol. 1, 2001, pp. 130 –134.
3. G. J. Dobeck and J. T. Cobb, “Fusion of multiple quadratic penalty function support vector machines (qpfsvm) for automated sea mine detection and classification,” in *Proceedings of the SPIE*, 2002, pp. 401–411. [Online]. Available: + http://dx.doi.org/10.1117/12.479112
4. J. T. Cobb and J. Principe, “Autocorrelation features for synthetic aperture sonar image seabed segmentation,” in *2011 IEEE International Conference on Systems, Man, and Cybernetics*, oct. 2011, pp. 3341 –3346.

5. ——, "Seabed segmentation in synthetic aperture sonar images," in *Proceedings of the SPIE*, 2011, pp. 80 170M–80 170M–11. [Online]. Available: + http://dx.doi.org/10.1117/12.883048
6. J. T. Cobb and A. Zare, "Multi-image texton selection for sonar image seabed co-segmentation," in *Proceedings of the SPIE*, 2013.
7. S. G. Kargl, K. L. Williams, and E. I. Thorsos, "Synthetic aperture sonar imaging of simple finite targets," *IEEE Journal of Oceanic Engineering*, vol. 37, no. 3, pp. 516–532, July 2012.
8. F. Langner, C. Knauer, W. Jans, and A. Ebert, "Side scan sonar image resolution and automatic object detection, classification and identification," *OCEANS 2009 EUROPE*, pp. 11–14, May 2009.
9. V. Myers and J. Fawcett, "A template matching procedure for automatic target recognition in synthetic aperture sonar imagery," *IEEE Signal Processing Letters*, vol. 17, no. 7, pp. 683–686, July 2010.
10. S. Guillaudeux, S. Daniel, and E. Maillard, "Optimization of a sonar image processing chain: A fuzzy rules based expert system approach," in *OCEANS'96. MTS/IEEE. Prospects for the 21st Century. Conference Proceedings*, vol. 3. IEEE, 1996, pp. 1319–1323.
11. F. Maussang, J. Chanussot, C. Hory, A. Hétet *et al.*, "Synthetic aperture sonar imagery: Towards a classification of under water mines in the mean-standard deviation plane," *Proc. Phys. Signal Image Process*, pp. 137–140, 2003.
12. F. Maussang, J. Chanussot, and A. Hétet, "Automated segmentation of sas images using the mean-standard deviation plane for the detection of underwater mines," in *OCEANS 2003. Proceedings*, vol. 4. IEEE, 2003, pp. 2155–2160.
13. F. Maussang, J. Chanussot, A. Hétet, and M. Amate, "Mean–standard deviation representation of sonar images for echo detection: Application to sas images," *Oceanic Engineering, IEEE Journal of*, vol. 32, no. 4, pp. 956–970, 2007.
14. F. Maussang, J. Chanussot, A. Hé, M. Amate *et al.*, "Higher-order statistics for the detection of small objects in a noisy background application on sonar imaging," *EURASIP Journal on Advances in Signal Processing*, vol. 2007, 2007.
15. D. P. Williams, "Unsupervised seabed segmentation of synthetic aperture sonar imagery via wavelet features and spectral clustering," in *Image Processing (ICIP), 2009 16th IEEE International Conference on*. IEEE, 2009, pp. 557–560.
16. J. T. Cobb and K. C. Slatton, "Dynamic tree segmentation of sonar imagery," in *Defense and Security Symposium*. International Society for Optics and Photonics, 2007, pp. 65 530P–65 530P.
17. ——, "A parameterized statistical sonar image texture model," in *SPIE Defense and Security Symposium*. International Society for Optics and Photonics, 2008, pp. 69 530K–69 530K.
18. J. T. Cobb, K. C. Slatton, and G. J. Dobeck, "A parametric model for characterizing seabed textures in synthetic aperture sonar images," *Oceanic Engineering, IEEE Journal of*, vol. 35, no. 2, pp. 250–266, 2010.
19. M. Mignotte, C. Collet, P. Perez, and P. Bouthemy, "Sonar image segmentation using an unsupervised hierarchical mrf model," *Image Processing, IEEE Transactions on*, vol. 9, no. 7, pp. 1216–1231, 2000.
20. S. Reed, Y. Petillot, and J. Bell, "An automatic approach to the detection and extraction of mine features in sidescan sonar," *Oceanic Engineering, IEEE Journal of*, vol. 28, no. 1, pp. 90–105, 2003.
21. ——, "Model-based approach to the detection and classification of mines in sidescan sonar," *Applied optics*, vol. 43, no. 2, pp. 237–246, 2004.
22. M. Mignotte, C. Collet, P. Pérez, and P. Bouthemy, "Hybrid genetic optimization and statistical model based approach for the classification of shadow shapes in sonar imagery," *Pattern Analysis and Machine Intelligence, IEEE Transactions on*, vol. 22, no. 2, pp. 129–141, 2000.
23. R. Fandos and A. M. Zoubir, "Optimal feature set for automatic detection and classification of underwater objects in sas images," *Selected Topics in Signal Processing, IEEE Journal of*, vol. 5, no. 3, pp. 454–468, 2011.
24. M. P. Hayes and P. T. Gough, "Synthetic aperture sonar: a review of current status," *Oceanic Engineering, IEEE Journal of*, vol. 34, no. 3, pp. 207–224, 2009.
25. A. E. Johnson and M. Hebert, "Seafloor map generation for autonomous underwater vehicle navigation," *Autonomous Robots*, vol. 3, no. 2-3, pp. 145–168, 1996.
26. E. Durá, J. Bell, and D. Lane, "Reconstruction of textured seafloors from side-scan sonar images," in *Radar, Sonar and Navigation, IEE Proceedings-*, vol. 151, no. 2. IET, 2004, pp. 114–126.

27. D. Jackson, “Models for scattering from the sea bed,” *PROCEEDINGS-INSTITUTE OF ACOUSTICS*, vol. 16, pp. 161–172, 1994.
28. D. Langer and M. Hebert, “Building qualitative elevation maps from side scan sonar data for autonomous underwater navigation,” in *Robotics and Automation, 1991. Proceedings., 1991 IEEE International Conference on*. IEEE, 1991, pp. 2478–2483.
29. R. Zhang, P.-S. Tsai, J. E. Cryer, and M. Shah, “Shape-from-shading: a survey,” *Pattern Analysis and Machine Intelligence, IEEE Transactions on*, vol. 21, no. 8, pp. 690–706, 1999.
30. J. Thomas, W. Kober, and F. Leberl, “Multiple image sar shape-from-shading,” *Photogrammetric Engineering and Remote Sensing*, vol. 57, no. 1, pp. 51–59, 1991.
31. G. McLachlan and T. Krishnan, *The EM algorithm and extensions*. John Wiley & Sons, 2007, vol. 382.
32. S. Z. Li and S. Singh, *Markov random field modeling in image analysis*. Springer, 2009, vol. 3.
33. J. Besag, “On the statistical analysis of dirty pictures,” *Journal of the Royal Statistical Society*, vol. 48, no. 3, pp. 259–302, 1986.
34. S. Geman and D. Geman, “Stochastic relaxation, gibbs distributions, and the bayesian restoration of images,” *Pattern Analysis and Machine Intelligence, IEEE Transactions on*, no. 6, pp. 721–741, 1984.
35. S. Z. Li, *Markov random field modeling in computer vision*. Springer-Verlag New York, Inc., 1995.
36. I. Dryden, L. Ippoliti, and L. Romagnoli, “Adjusted maximum likelihood and pseudo-likelihood estimation for noisy gaussian markov random fields,” *Journal of Computational and Graphical Statistics*, vol. 11, no. 2, 2002.
37. J. Besag, “Statistical analysis of non-lattice data,” *The statistician*, pp. 179–195, 1975.
38. ——, “Efficiency of pseudolikelihood estimation for simple gaussian fields,” *Biometrika*, pp. 616–618, 1977.
39. T. Burr and A. Skurikhin, “Pseudo-likelihood inference for gaussian markov random fields,” *Statistics Research Letters*, vol. 2, no. 3, 2013.
40. S. Foucher, M. Germain, J.-M. Boucher, and G. B. Benie, “Multisource classification using icm and dempster-shafer theory,” *IEEE Transactions on Instrumentation and Measurement*, vol. 51, no. 2, pp. 277–281, 2002.
41. J. Besag, “Spatial interaction and the statistical analysis of lattice systems,” *Journal of the Royal Statistical Society. Series B (Methodological)*, pp. 192–236, 1974.